Three-Photon-Excited Luminescence from Unsymmetrical Cyanostilbene Aggregates: Morphology Tuning and Targeted Bioimaging

Amal Kumar Mandal,[†,Δ] Sivaramapanicker Sreejith,[†,Δ] Tingchao He,[‡,Δ] Swarup Kumar Maji,[†] Xiao-Jun Wang,[†] Shi Li Ong,[†] James Joseph,[†] Handong Sun,[*,§] and Yanli Zhao[*,†,¶]

[†]Division of Chemistry and Biological Chemistry, School of Physical and Mathematical Sciences and [§]Division of Physics and Applied Physics, Centre for Disruptive Photonic Technologies (CDPT), School of Physical and Mathematical Sciences, Nanyang Technological University, 21 Nanyang Link 637371, Singapore, [‡]College of Physics Science & Technology, Shenzhen University, Shenzhen 518060, China, and [¶]School of Materials Science and Engineering, Nanyang Technological University, 639798 Singapore. [Δ]These authors (A.K.M., S.S., and T.H.) contributed equally to this work.

ABSTRACT We report an experimental observation of aggregation-induced enhanced luminescence upon three-photon excitation in aggregates formed from a class of unsymmetrical cyanostilbene derivatives. Changing side chains ($-CH_3$, $-C_6H_{13}$, $-C_7H_{15}O_3$, and folic acid) attached to the cyanostilbene core leads to instantaneous formation of aggregates with sizes ranging from micrometer to nanometer scale in aqueous conditions. The crystal structure of a derivative with a methyl side chain reveals the planarization in the unsymmetrical cyanostilbene core, causing luminescence from corresponding aggregates upon three-photon excitation. Furthermore, folic acid attached cyanostilbene forms well-dispersed spherical nanoaggregates that show a high three-photon cross-section of 6.0×10^{-80} cm^6 s^2 $photon^{-2}$ and high luminescence quantum yield in water. In order to demonstrate the targeted bioimaging capability of the nanoaggregates, three cell lines (HEK293 healthy cell line, MCF7 cancerous cell line, and HeLa cancerous cell line) were employed for the investigations on the basis of their different folate receptor expression level. Two kinds of nanoaggregates with and without the folic acid targeting ligand were chosen for three-photon bioimaging studies. The cell viability of three types of cells incubated with high concentration of nanoaggregates still remained above 70% after 24 h. It was observed that the nanoaggregates without the folic acid unit could not undergo the endocytosis by both healthy and cancerous cell lines. No obvious endocytosis of folic acid attached nanoaggregates was observed from the HEK293 and MCF7 cell lines having a low expression of the folate receptor. Interestingly, a significant amount of endocytosis and internalization of folic acid attached nanoaggregates was observed from HeLa cells with a high expression of the folate receptor under three-photon excitation, indicating targeted bioimaging of folic acid attached nanoaggregates to the cancer cell line. This study presents a paradigm of using organic nanoaggregates for targeted three-photon bioimaging.

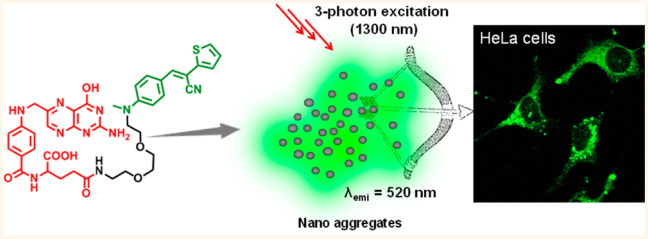

KEYWORDS: aggregation-induced enhanced luminescence · cyanostilbene · folic acid · targeted bioimaging · three photon

Optical imaging techniques present capabilities to probe into critical molecular processes in active biological specimens using advanced instrumentation schemes and suitable contrast agents.[1−4] Although optical imaging provides better resolution in visualization of cells and tissues at shallow depths, the resolution decreases rapidly as a function of the imaging depth.[5,6] The bottleneck problems in optical imaging such as the scattering of light owing to tissue heterogeneity and the difficulty in obtaining high-resolution images could be overcome by using near-infrared (NIR) light in the second NIR window of 1.0−1.4 μm in the electromagnetic spectrum.[7−15] An effective way to achieve this strategy for bioimaging and sensing applications is to utilize a three-photon excitation (3PE) process. The main advantage of the 3PE process is its significant improvement in the overall excitation localization as a result of improving the signal-to-background ratio (SBR) when compared to one- and two-photon excitations.[16−19] The

* Address correspondence to zhaoyanli@ntu.edu.sg, hdsun@ntu.edu.sg.

Received for review June 12, 2014 and accepted May 7, 2015.

Published online May 07, 2015
10.1021/nn507072r

fluorescence of 3PE falls off as $\sim 1/z^4$ (where z is the distance from the focal plane), whereas the fluorescence of two-photon excitation falls off as $\sim 1/z^2$. Therefore, 3PE dramatically reduces the out-of-focus background in regions far from the focal plane, improving the SBR by orders of magnitude when compared to two-photon excitation. For example, Horton *et al.* compared the SBR between a three-photon microscope and a two-photon microscope under the same excitation wavelength, showing that three-photon microscope imaging could afford ~4.5 orders of improvement in the SBR over two-photon microscope imaging upon excitation at 1280 nm.[20]

To date, there are only a few studies reporting three-photon excited bioimaging by employing organic dyes such as Texas red[20] and inorganic quantum dots (QDs).[21] However, these platforms are challenged with the tendency for nonemissive aggregate formation in aqueous solution, high toxicity, and low three-photon absorption (3PA) cross-section. For instance, the presence of inherently toxic elements (*e.g.*, cadmium and selenium) in QDs makes the nanoparticles toxic to cell lines and live animals.[22−26] Recently, Yong *et al.* reviewed the toxicity of various QDs, indicating that intracellular uptake of QDs could disturb the oxidative balance of cells and cause oxidative stress.[27] At a high level of oxidative stress, the antioxidant defense system is overwhelmed, eventually leading to mitochondrial malfunctions as well as apoptosis. The oxidative stress could also interfere with DNA functions, causing genotoxicity and neurotoxicity.[28] Furthermore, heavy metal cores of QDs might have a possibility of being degraded in a biological environment during their interactions with intracellular thiols or under UV excitation,[29,30] resulting in undesired cytotoxicity, unwanted aggregation, and unstable fluorescence signals.[23,31] In comparison to QDs, isolated organic fluorophores such as Texas red usually show low fluorescence and photobleaching in aqueous conditions, which greatly compromises their performance.[32−34] Thus, novel organic fluorophores capable of forming nanoparticles with superior biocompatibility and strong three-photon excited luminescence have been sought after for bioimaging.

In the past few years, luminescent organic nanoaggregates have received considerable attention owing to their size-dependent optoelectronic properties, which show significant application potential in areas such as biological imaging and sensing.[35−37] Such nanoaggregates are quite unique on account of their small size and robustness, while the surface modification and morphology tuning allow their binding affinity to be tailored toward various biological applications serving as imaging probes and drug delivery vehicles.[38−41] To the best of our knowledge, however, there were no organic fluorophore-based nanoaggregates fabricated for bioimaging in the NIR region using 3PE, and there was also no study to investigate the effect of side chains on the morphology change and controlled formation of organic nanoaggregates for targeted NIR bioimaging.

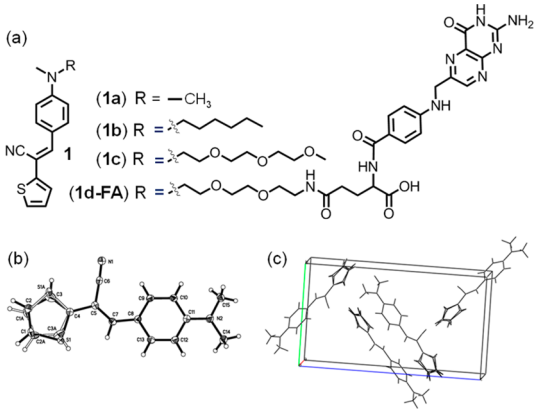

Figure 1. (a) Molecular structures of unsymmetrical cyanostilbene derivatives 1a−c and 1d-FA. (b) Single-crystal ORTEP diagram of 1a. (c) Crystal packing structure of 1a.

Herein, we report a new class of unsymmetrical cyanostilbene derivatives (Figure 1) that exhibit tunable morphology and remarkable 3PA cross sections upon the formation of nanoaggregates in aqueous−organic mixture solution. In our design, we varied side chains from hydrophobic ($-CH_3$ and $-C_6H_{13}$) to hydrophilic ($-C_7H_{15}O_3$ glycol and folic acid (FA) attached glycol) units substituted on the *N*-atom of unsymmetrical cyanostilbene, leading to the formation of derivatives **1a**−**c** and **1d-FA** accordingly. Tuning the morphology of formed aggregates from random to well-ordered superstructures was achieved in a dimethyl sulfoxide (DMSO)/water mixture solvent. Derivatives **1c** and **1d-FA** with hydrophilic side chains preferably formed well-dispersed spherical nanoaggregates ($\mathbf{1c}_{(agg)}$ and $\mathbf{1d\text{-}FA}_{(agg)}$). We experimentally observed unprecedented aggregation-induced enhanced luminescence excited by 3PA from the nanoaggregates of **1a**−**c** and **1d-FA**. A comparative study was carried out using nanoaggregates $\mathbf{1c}_{(agg)}$ and $\mathbf{1d\text{-}FA}_{(agg)}$ in three different cell lines, including HEK293 (healthy human embryonic kidney 293 cell line with a low level of folate receptor expression), MCF7 (breast cancer cell line with a low level of folate receptor expression), and HeLa (cervical cancer cell line with a high level of folate receptor expression). Three-photon imaging was conducted *in vitro* using these healthy and cancerous cell lines to confirm folate receptor-mediated endocytosis and subsequent enhanced internalization of nanoaggregate $\mathbf{1d\text{-}FA}_{(agg)}$ in HeLa cells when compared to nanoaggregate $\mathbf{1c}_{(agg)}$.

RESULTS AND DISCUSSION

The synthesis of unsymmetrical cyanostilbene derivatives **1a**−**c** and **1d-FA** was carried out by typical Knoevenegal-type condensation of corresponding aldehydes with 2-thiopheneacetonitrile in 40−70% yields. General multistep synthetic procedures for the

preparation of compounds **1a**−**c** and **1d-FA** were described in the Supporting Information (SI, Figures S1 and S2). All of the compounds were thoroughly characterized using standard techniques. Single crystals of **1a** with a methyl side chain (−CH_3) were obtained by slow vapor diffusion of chloroform/hexane mixture solution for X-ray diffraction studies. It was observed that the obtained yellow crystals of **1a** exhibit green luminescence upon 365 nm light irradiation (Figure S3, SI). A neat crystal of **1a** was chosen for data collection, and the corresponding ORTEP diagram and crystal-packing structure are shown in Figure 1. The details of crystal data and structural refinement are provided in the SI (Tables S1−S3). The crystal structure of **1a** has an orthorhombic system (space group of $P2_{(1)}2_{(1)}2_{(1)}$) with four molecules in the unit cell (Figure 1c). Structural analysis reveals that there is a small dihedral angle of 1.1° between the planes of the benzene ring and adjacent thiophene unit. Apparently, the observation suggests that **1a** undergoes planarization in the solid state in order to maximize the extended π-conjugation as well as the dipolar nature of the molecule.

Compounds **1a**−**c** and **1d-FA** showed absorption maxima centered at 421, 414, 407, and 390 nm in DMSO, respectively (Table 1 and Figure S4, SI). Interestingly, **1a**−**c** and **1d-FA** exhibited no emission in any of organic solvents such as $CHCl_3$, tetrahydrofuran, acetonitrile, and DMSO. On the basisi of the luminescence observed from the crystals of **1a**, it was expected that the aggregation formation might lead to the enhanced luminescence from compounds **1a**−**c** and **1d-FA**. To investigate the aggregation process, the DMSO/water mixture solvent was used for the analysis. Upon increasing the percentage of water in DMSO solutions of **1a**−**c** and **1d-FA**, the absorption of all four derivatives decreased, indicating the aggregation formations (Figure S4, SI).[42−44]

Furthermore, we measured the luminescence spectra (Figure 2) of aggregates formed from all the derivatives in DMSO/water mixture solution by varying the fraction of water (f_w). In pure DMSO, no luminescence emission was observed for all the derivatives. Dramatic increases in luminescence intensity were observed for all derivatives upon increasing the percentage of water content in DMSO. When f_w was 60 vol % in DMSO, **1a** showed an obvious formation of well-dispersed aggregates with a luminescence enhancement at 520 nm. Increasing f_w to 90 vol % for **1a** in DMSO led to the formation of precipitates (Figure 2a). Compounds **1b**,**c** and **1d-FA** exhibited the maximum luminescence enhancement upon increasing f_w to 90 vol % in DMSO (Figure 2d,g,j). A summary of photophysical properties of compounds **1a**−**c** and **1d-FA** was tabulated in Table 1. For aggregate **1a**$_{(agg)}$, a substantial increment of luminescence quantum yield (Φ = 0.62) was achieved at a water fraction of f_w = 60 vol % as compared to f_w = 0 vol %. In the case of aggregate **1b**$_{(agg)}$, an 80-fold increase in the luminescence intensity with quantum yield of Φ = 0.42 was observed at f_w = 90 vol % when compared to f_w = 0 vol %. For **1c**$_{(agg)}$ and **1d-FA**$_{(agg)}$, 60- and 42-fold increases in the luminescence intensity with quantum yields of Φ = 0.32 and 0.31 were achieved at a water fraction of f_w = 90 vol % as compared to f_w = 0 vol %, respectively.

TABLE 1. Summary of Photophysical Properties of Compounds 1a−c and 1d-FA in DMSO as Well as Aggregates 1a$_{(agg)}$, 1b$_{(agg)}$, 1c$_{(agg)}$, and 1d-FA$_{(agg)}$ in DMSO/Water Mixture Solution

sample	λ_{abs}[a] (nm)	λ_{em}[a] (nm)	ε[a] (10^3 M^{-1} cm^{-1})	Φ[b] (%)	τ[c] (ns)
1a	421		29.24		
1a$_{(agg)}$	417	520	7.66	62	0.34
1b	414		20.66		
1b$_{(agg)}$	405	527	15.79	42	0.14
1c	407		15.10		
1c$_{(agg)}$	397	532	9.42	32	0.52
1d-FA	390		10.36		
1d-FA$_{(agg)}$	377	516	7.41	31	2.44

[a] Determined using spectroscopic-grade DMSO and Millipore water. [b] Luminescence quantum yields (±5% error) were determined using quinine sulfate as the standard (Φ_f = 0.54 in 0.1 M H_2SO_4). [c] Excited state lifetimes were measured through monoexponential convolution fit on the fluorescence decay profile. The fitting decays were judged through the reduced χ^2 values. The fits were accepted for χ^2 = 0.8−1.2.

We then investigated in detail the morphology of the aggregates **1a**$_{(agg)}$, **1b**$_{(agg)}$, **1c**$_{(agg)}$, and **1d-FA**$_{(agg)}$ in a DMSO/water mixture solvent using transmission electron microscopy (TEM). Well-dispersed aggregates were prepared on the basis of previously reported procedures.[45,46] Parts a−d of Figure 3 show representative TEM images of the corresponding aggregates. Clearly, **1a**$_{(agg)}$ exhibits random and extended aggregate formation without any distinct morphological features due to its high hydrophobic nature (Figure 3a). Owing to the attachment of a hydrophobic side chain in **1b**$_{(agg)}$, vascular-like structures with a wide range of particle size distributions were observed (Figure 3b). In this case, the hydrophobic side chain may prevent extended aggregation, which leads to segmented aggregates within submicrometer size range. Interestingly, **1c**$_{(agg)}$ and **1d-FA**$_{(agg)}$ showed solid spherical nanoparticles with an average diameter of 150 nm. The formation of spherical morphology for **1c**$_{(agg)}$ and **1d-FA**$_{(agg)}$ indicates the possibility of a rapid assembly of hydrophobic unsymmetrical cyanostilbene cores facing toward the center of the spheres covered with hydrophilic glycol as well as FA-attached glycol side chains (Figure 3c,d). The particle size distribution was also investigated by dynamic light scattering (DLS), indicating a wide range of particle size distribution for **1b**$_{(agg)}$ with an average diameter of 342 nm (Figure 3e). Similarly, the nanoaggregates formed by **1c**$_{(agg)}$ and **1d-FA**$_{(agg)}$ show average diameters of 164 and 195 nm, respectively (Figure 3f,g). The average hydrodynamic diameters measured from DLS study for

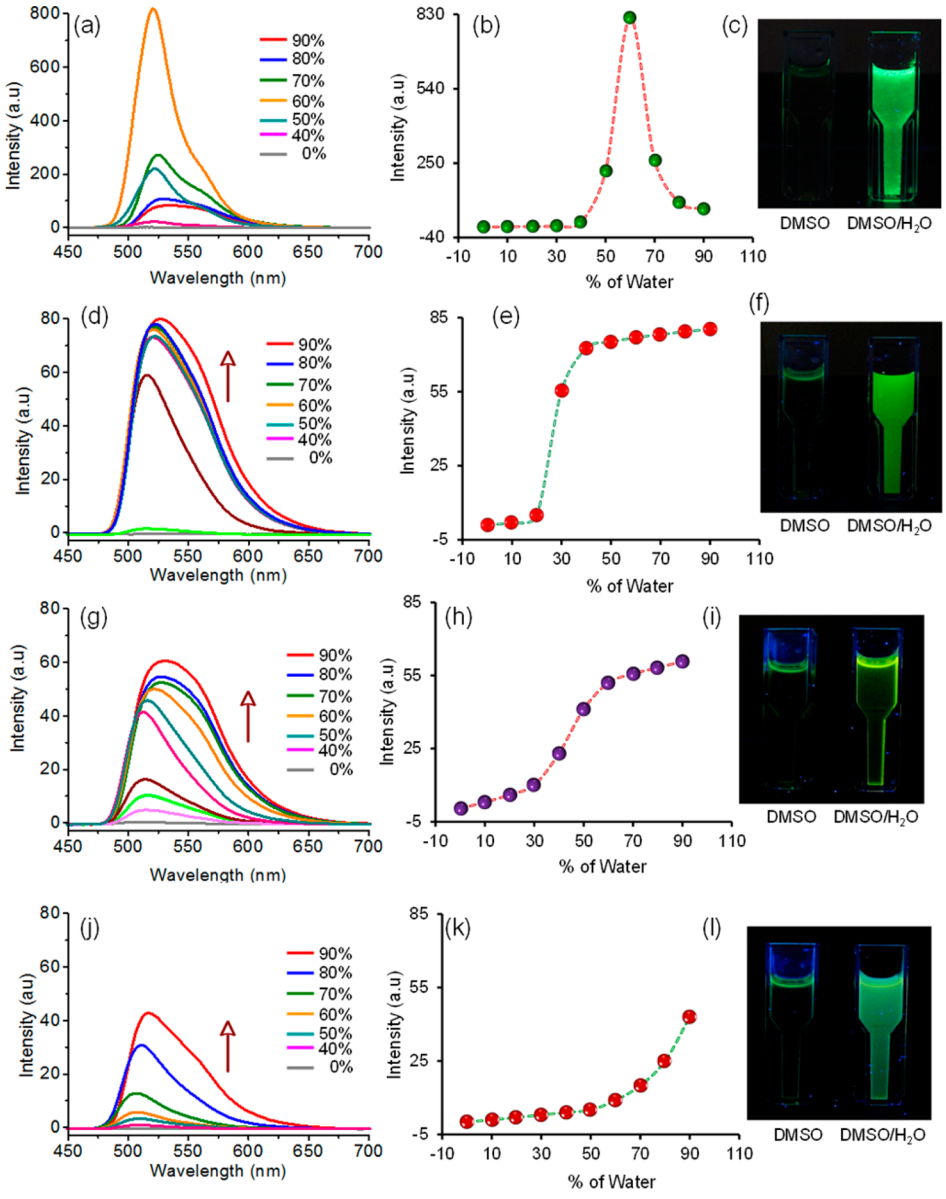

Figure 2. (a, d, g, j) Fluorescence spectra of compounds 1a−c and 1d-FA (5.0×10^{-5} M) recorded in DMSO with increasing water contents, respectively. All of the spectra were recorded under excitation of 425 nm at room temperature. The colored lines indicate the volume percentage of water during the measurements. (b, e, h, k) Corresponding plots of emission intensity changes versus water contents for 1a−c and 1d-FA, respectively. (c, f, i, l) Visual color changes for the compounds 1a−c and 1d-FA taken under illumination with 365 nm UV light, respectively.

1c$_{(agg)}$ and **1d-FA**$_{(agg)}$ were in good agreement with the particle sizes obtained from the TEM analysis. Thus, the morphological analysis by TEM and DLS confirms the morphology tuning in a wide range of nanometer scale through changing the side chains on the unsymmetrical cyanostilbene backbone of **1a**$_{(agg)}$, **1b**$_{(agg)}$, **1c**$_{(agg)}$, and **1d-FA**$_{(agg)}$ in DMSO/water conditions.

In order to study the stability of the aggregates, well-dispersed suspensions of aggregates were allowed to store in the dark at room temperature for 2 weeks and then were analyzed using TEM. No difference in the particle size was found for both **1c**$_{(agg)}$ and **1d-FA**$_{(agg)}$, and the precipitates were observed for the case of **1b**$_{(agg)}$. Furthermore, we investigated the luminescence stability of **1c**$_{(agg)}$ and **1d-FA**$_{(agg)}$ in the cell culture medium, *i.e.*, Dulbecco's Modified Eagle Medium (DMEM) supplemented with 10% fetal bovine serum. The luminescence intensity of **1c**$_{(agg)}$ and **1d-FA**$_{(agg)}$ remained 92% and 93% of their initial values after 7-day incubation at 37 °C (Figure S7, SI), indicating the good stability of the nanoaggregates for the following biological studies.

As a strong one-photon excited luminescence enhancement was observed in aggregates **1a**$_{(agg)}$, **1b**$_{(agg)}$, **1c**$_{(agg)}$, and **1d-FA**$_{(agg)}$, we extended the investigation to 3PE in the NIR region. Interestingly, unprecedented enhanced luminescence upon 3PE at 1300 nm was observed in DMSO/water mixture solution for all

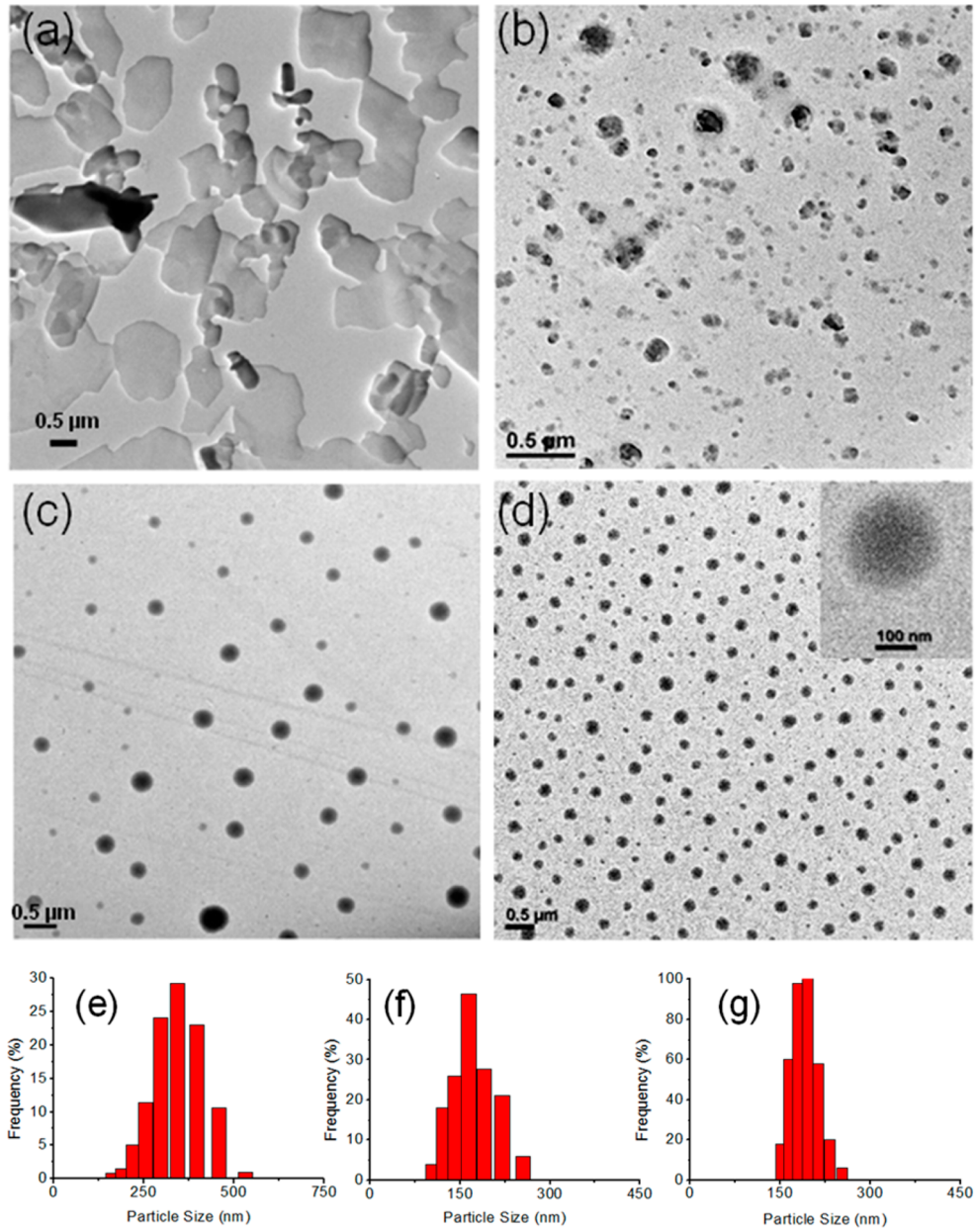

Figure 3. TEM images of (a) $1a_{(agg)}$, (b) $1b_{(agg)}$, (c) $1c_{(agg)}$, and (d) $1d\text{-}FA_{(agg)}$. The nanoaggregates $1b_{(agg)}$, $1c_{(agg)}$, and $1d\text{-}FA_{(agg)}$ were prepared by injecting the concentrated solution of corresponding compounds in DMSO (4.0×10^{-3} M, 50 μL) into water (3.95 mL). The final concentration is 5.0×10^{-5} M, and the proportion of DMSO in water is 1.25 vol %. For compound 1a, the aggregates were prepared by injecting the concentrated solution of the compound (1.25×10^{-4} M, 1.6 mL) in DMSO into water (2.4 mL). The final concentration is 5.0×10^{-5} M, and the proportion of DMSO in water is 40 vol %. DLS particle size distribution plots of (e) $1b_{(agg)}$ (PDI = 0.245), (f) $1c_{(agg)}$ (PDI = 0.152), and (g) $1d\text{-}FA_{(agg)}$ (PDI = 0.175).

aggregates. An optimized aggregate concentration of 5.0×10^{-5} M was used after several trials based on photophysical experiments. Three-photon luminescence spectra (Figure 4) measured for **1a**$_{(agg)}$, **1b**$_{(agg)}$, **1c**$_{(agg)}$, and **1d-FA**$_{(agg)}$ showed no obvious difference in comparison with their one-photon luminescence, indicating that the same fluorescent state was reached regardless of the excitation mode. The logarithmic plots of photoluminescence intensity as a function of incident power with a slope of about 3 for **1a**$_{(agg)}$, **1b**$_{(agg)}$, **1c**$_{(agg)}$, and **1d-FA**$_{(agg)}$ further confirm the three-photon emission process (Figure 4c). Parts d–g of Figure 4 show photographs of the three-photon aggregation-induced luminescence observed for **1a**$_{(agg)}$, **1b**$_{(agg)}$, **1c**$_{(agg)}$, and **1d-FA**$_{(agg)}$ in DMSO/water mixture solution, respectively.

3PA cross-sections of the samples were determined by multiphoton excited luminescence method using rhodamine B as the reference. A summary of the corresponding values of the three-photon cross-section and action cross-section for **1a**$_{(agg)}$, **1b**$_{(agg)}$, **1c**$_{(agg)}$, and **1d-FA**$_{(agg)}$ is shown in Table 2. The highest 3PA cross-section was observed for **1d-FA**$_{(agg)}$ with $\sigma_3 = 6.0 \times 10^{-80}$ cm^6 s^2 photon^{-2}, which gives the action

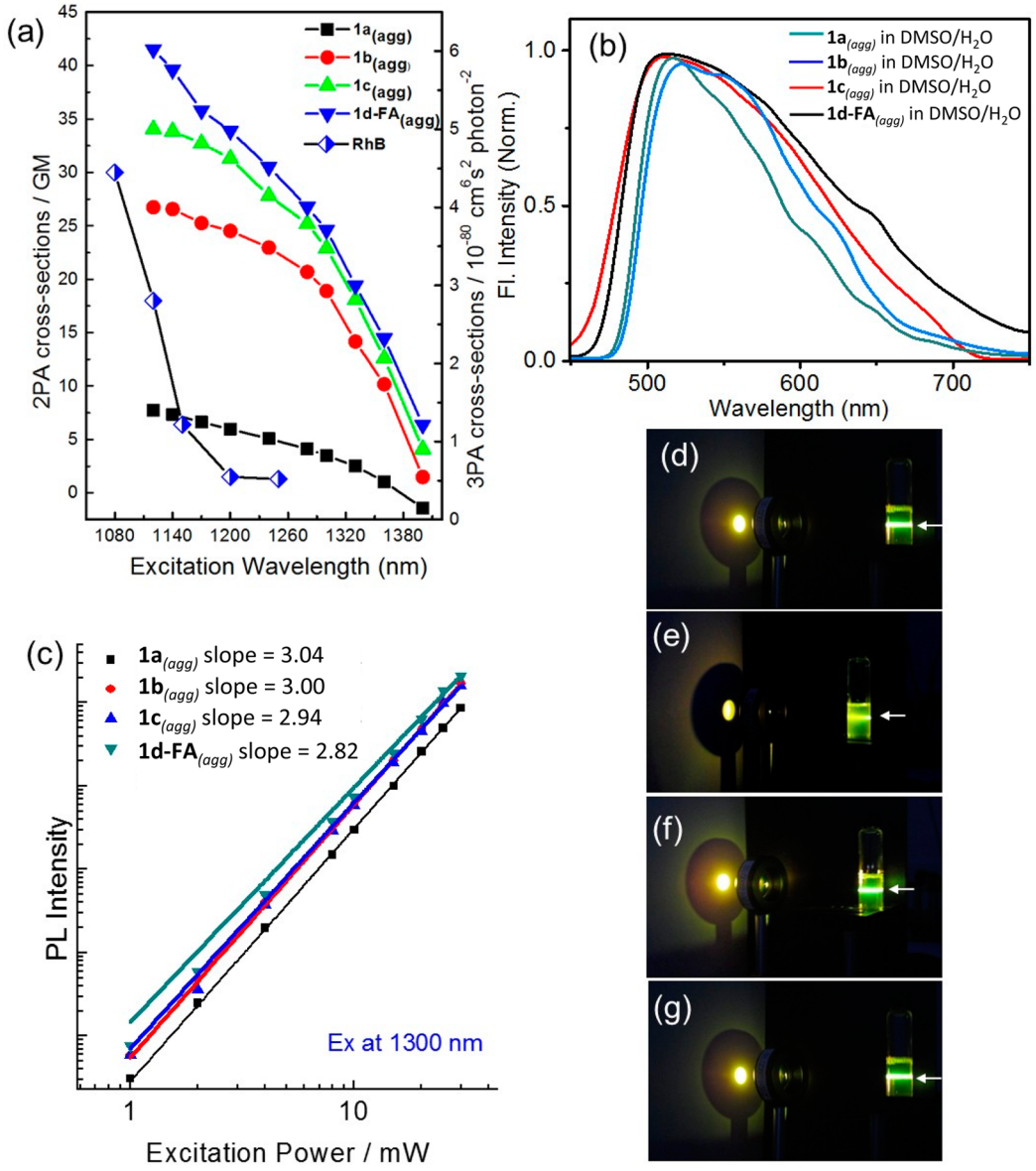

Figure 4. (a) 3PA spectra of $1a_{(agg)}$ in DMSO/water mixture (4:6 v/v) and $1b_{(agg)}$, $1c_{(agg)}$, and $1d\text{-}FA_{(agg)}$ in DMSO/water mixture (1:9 v/v) at a concentration of 5.0×10^{-5} M, as well as 2PA spectrum of rhodamine B in water. (b) Corresponding three-photon excited luminescence spectra of $1a_{(agg)}$, $1b_{(agg)}$, $1c_{(agg)}$, and $1d\text{-}FA_{(agg)}$ under excitation of $\lambda_{exc} = 1300$ nm. (c) Logarithmic plot of luminescence output versus incident power intensity for $1a_{(agg)}$, $1b_{(agg)}$, $1c_{(agg)}$, and $1d\text{-}FA_{(agg)}$. Photographs showing three-photon images from (d) $1a_{(agg)}$, (e) $1b_{(agg)}$, (f) $1c_{(agg)}$, and (g) $1d\text{-}FA_{(agg)}$ reflected on a white screen for clarity. White arrows indicate the direction of incident laser beam.

cross-section ($\eta_3\sigma_3$) of 1.9×10^{-80} cm^6 s^2 photon^{-2}. The reported 3PA cross-section value here is obviously higher than some previously reported dyes. For example, Xu *et al.* measured the 3PA action cross-section of some organic dyes like DNA stain 4′,6-diamidino-2-phenylindole ($\sigma_3 = 2.5 \times 10^{-84}$ cm^6 s^2 photon^{-2}), dansyl hydrazine ($\sigma_3 = 3.0 \times 10^{-84}$ cm^6 s^2 photon^{-2}), as well as Ca^{2+} indicators indo-1 ($\sigma_3 = 2.0 \times 10^{-83}$ cm^6 s^2 photon^{-2}) and fura-2 ($\sigma_3 = 2.0 \times 10^{-82}$ cm^6 s^2 photon^{-2}) in buffered solution at pH 7.2.[8] Maiti and co-workers reported the 3PA cross-section of tyrosine ($\sigma_3 = 1.0 \times 10^{-84}$ cm^6 s^2 photon^{-2}), tryptophan ($\sigma_3 = 1.0 \times 10^{-84}$ cm^6 s^2 photon^{-2}), and serotonin ($\sigma_3 = 4.0 \times 10^{-84}$ cm^6 s^2 photon^{-2}) in aqueous buffer.[10] Zipfel *et al.* reported the 3PA cross-section of some intrinsic emitters such as melatonin ($\sigma_3 = 7.0 \times 10^{-84}$ cm^6 s^2 photon^{-2}), 5-HIAA ($\sigma_3 = 2.0 \times 10^{-84}$ cm^6 s^2 photon^{-2}), and 5-HTOL ($\sigma_3 = 5.0 \times 10^{-84}$ cm^6 s^2 photon^{-2}).[11] Cohanoschi *et al.* reported a very high 3PA cross-section ($\sigma_3 = 2.5 \times 10^{-71}$ cm^6 s^2 photon^{-2}) of pseudoisocyanine in its *J*-aggregated form at very high concentration (2.0×10^{-3} M), while no experimental evidence of pure 3PA in the monomer was observed.[47] Wu *et al.* reported the 3PA cross-section of a series of 1,2,4-triazole end-capped oligofluorene derivatives in toluene. They showed that the 3PA cross-section value increased from $\sigma_3 = 1.8 \times 10^{-80}$ cm^6 s^2 photon^{-2} to

TABLE 2. Summary of 3PA Parameters for Aggregates $\mathbf{1a}_{(agg)}$, $\mathbf{1b}_{(agg)}$, $\mathbf{1c}_{(agg)}$, and $\mathbf{1d\text{-}FA}_{(agg)}$[a]

aggregate[b]	σ_3 (cm^6 s^2 photon^{-2})	$\eta_3\sigma_3$[c] (cm^6 s^2 photon^{-2})	slope[d]
$\mathbf{1a}_{(agg)}$	1.3×10^{-80}	0.8×10^{-80}	3.04
$\mathbf{1b}_{(agg)}$	4.0×10^{-80}	1.7×10^{-80}	3.00
$\mathbf{1c}_{(agg)}$	5.0×10^{-80}	1.6×10^{-80}	2.94
$\mathbf{1d\text{-}FA}_{(agg)}$	6.0×10^{-80}	1.9×10^{-80}	2.82

[a] Maximum 3PA cross-section (σ_3) and action cross-section ($\eta_3\sigma_3$) along with the slope values of logarithmic plots of luminescence output *versus* laser power are shown. [b] All measurements were carried out using DMSO/water mixture solvent (**1a**: 4:6 v/v; **1b**, **1c**, and **1d-FA**: 1:9 v/v). [c] η_3 denotes luminescence quantum efficiency by assuming that one- and three-photon excited luminescence quantum efficiency remains the same. [d] Slopes were measured at $I_{peak} = \sim 100$ GW/cm^2.

$\sigma_3 = 2.4 \times 10^{-78}$ cm^6 s^2 photon^{-2} upon introduction of two more oligofluorene units in the backbone.[48] As compared with these reported systems, the present nanoaggregate $\mathbf{1d\text{-}FA}_{(agg)}$ was prepared in water-containing solution, showing cancer cell-targeted bioimaging capability as discussed later.

Previous theoretical calculations on the 3PA cross-section of organic molecules revealed that the transition dipole moment between the ground state and the final state is the only parameter contributing to the final 3PA cross-section.[49] This conclusion suggests that functionalizing molecules with an electron-donating or -accepting unit to expand the conjugation could lead to better charge separation to improve the cross-section value.[50] Another possible way is to facilitate excitonic coupling and intermolecular interactions, where monomers with a relatively simple structure are capable of self-assembly to form aggregates.[51−53] Thus, for nanoaggregates $\mathbf{1a}_{(agg)}$, $\mathbf{1b}_{(agg)}$, $\mathbf{1c}_{(agg)}$, and $\mathbf{1d\text{-}FA}_{(agg)}$, the observed enhancement in cross-section value could be attributed to intermolecular cooperative effects due to the aggregation, which include the contributions from planarization induced extended π-conjugation of the cyanostilbene core, polarizability, and donor−acceptor−donor interactions.[54,55] On the other hand, since a large number of cyanostilbene molecules are in the aggregated state with parallel dipole moment, the electronic transition of individual molecule is strongly coupled by the excitonic interaction, leading to an enormous transition dipole moment. Similarly, the donor-π-acceptor structure along with four oligofluorene derivatives further extends the conjugation and charge separation in nonaqueous solvent, which is responsible for higher cross-section value[48] as compared to our measured value.

Thus, the large 3PA cross-section along with high stability and brightness from $\mathbf{1c}_{(agg)}$ and $\mathbf{1d\text{-}FA}_{(agg)}$ encourages us to carry out targeted three-photon imaging *in vitro*. In order to demonstrate the targeted bioimaging capability, three different cell lines (HEK293 healthy cell line, MCF7 cancerous cell line, and HeLa cancerous cell line) were selected according to their folate receptor expression level. Among them,

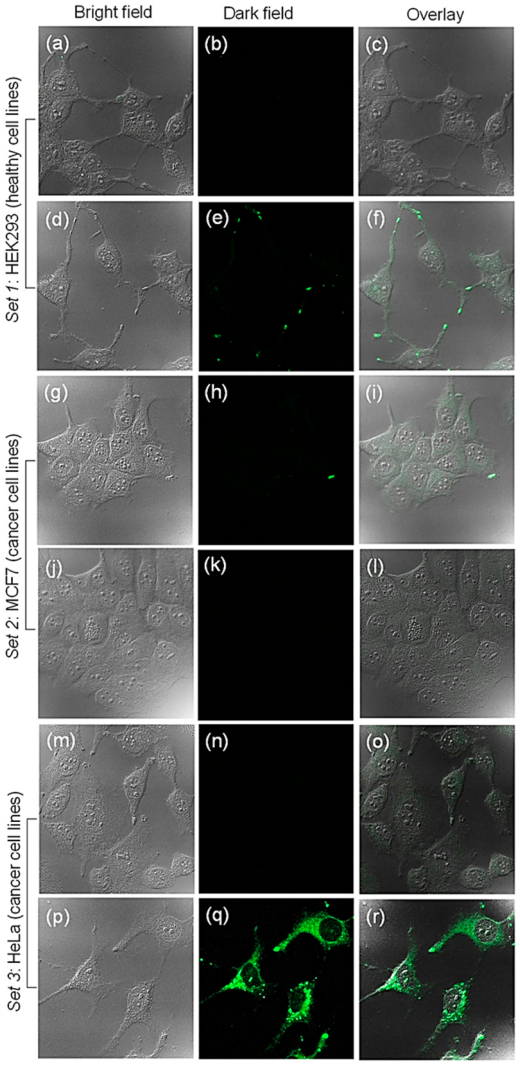

Figure 5. Three-photon microscopy images of HEK293 (a−f), MCF7 (g−l), and HeLa (m−r) cells incubated with $\mathbf{1c}_{(agg)}$ and $\mathbf{1d\text{-}FA}_{(agg)}$ for 4 h. Set 1: HEK293 healthy cells, (a−c) for $\mathbf{1c}_{(agg)}$ and (d−f) for $\mathbf{1d\text{-}FA}_{(agg)}$. Set 2: MCF7 cancer cells, (g−i) for $\mathbf{1c}_{(agg)}$ and (j−l) for $\mathbf{1d\text{-}FA}_{(agg)}$. Set 3: HeLa cancer cells, (m−o) for $\mathbf{1c}_{(agg)}$ and (p−r) for $\mathbf{1d\text{-}FA}_{(agg)}$. Excitation λ_{exc} was at 1300 nm, and emission was collected at 500−600 nm.

the HeLa cell line is well-known for its high expression of the folate receptor as a positive control (FA+), whereas MCF7 and HEK293 cell lines have a low expression of the folate receptor as negative controls (FA-).[56,57] Two different nanoaggregates $\mathbf{1d\text{-}FA}_{(agg)}$ with an FA side chain and $\mathbf{1c}_{(agg)}$ without an FA side chain were chosen for the comparison of targeted bioimaging. The inherent cytotoxicity of $\mathbf{1c}_{(agg)}$ and $\mathbf{1d\text{-}FA}_{(agg)}$ was evaluated using 3-(4,5-dimethlthiazol-2-yl)-2,5-diphenyltetrazolium bromide (MTT) assay in the three types of cell lines. The cell viability of HeLa cell line remained over 70% after 24 h incubation with high concentrations (760 μM) of $\mathbf{1c}_{(agg)}$ and $\mathbf{1d\text{-}FA}_{(agg)}$. Similarly, for MCF7 and HEK293 cell lines, the viability remained 74% and 81% for $\mathbf{1c}_{(agg)}$ and 87% and 90% for $\mathbf{1d\text{-}FA}_{(agg)}$ under the same conditions, respectively

(Figures S8−S10, SI). Evidently, both **1c**$_{(agg)}$ and **1d-FA**$_{(agg)}$ exhibited low toxicity even at very high concentrations, further proving their suitability for bioimaging.

We then demonstrated the three-photon bioimaging capability of **1c**$_{(agg)}$ and **1d-FA**$_{(agg)}$ using HEK293, HeLa, and MCF7 cell lines, and a schematic diagram of the microscopy setup is shown in Figure S11 (SI). All of the cell lines were incubated with **1c**$_{(agg)}$ and **1d-FA**$_{(agg)}$ in respective sets for 4 h. An aggregate concentration of 47.5 μM was used after optimization by several trials in order to achieve uniform distribution of aggregates for bioimaging. Nanoaggregate **1c**$_{(agg)}$ with a glycol side chain did not undergo the endocytosis by both healthy and cancerous cell lines within the incubation time. FA attached **1d-FA**$_{(agg)}$ exhibited targeted endocytosis to HeLa cells with high FA receptor expression. Figure 5 shows the results of the three-photon bioimaging experiments upon excitation at 1300 nm and emissions collected at 500−600 nm. Figure 5a−c, Figure 5g−i, and Figure 5m−o are the images of **1c**$_{(agg)}$-incubated cell lines for 4 h. Clearly, no endocytosis was observed in the three cell lines. Figure 5d−f, Figure 5j−l, and Figure 5p−r present the images of **1d-FA**$_{(agg)}$ incubated cell lines for 4 h. For HEK293 and MCF7 cells, no obvious endocytosis of **1d-FA**$_{(agg)}$ was observed. Interestingly, enhanced endocytosis of **1d-FA**$_{(agg)}$ was observed in HeLa cancer cells, which was clearly evidenced from both the dark field (Figure 5q) and overlay (Figure 5r) images. As compared with bioimaging results under one- and two-photon excitations (Figures S12 and S13 in the SI), the obtained three-photon bioimaging showed better performance. On the other hand, the present imaging resolution is relatively lower than previously reported case.[21] Since nanoaggregate **1d-FA**$_{(agg)}$ consists of cyanostilbene fluorophores, its imaging performance may vary upon a slight change in the aggregate dimension. In such an organic system, the amount of 3PA may show slight variations with a decrease in the image resolution. Nevertheless, these experiments proved targeted bioimaging of **1d-FA**$_{(agg)}$ under three-photon luminescence for the first time.

CONCLUSIONS

In conclusion, we present the development of a new class of unsymmetrical cyanostilbenes (**1a**−**c** and **1d-FA**) and their unprecedented aggregates with multiphoton properties. We have observed aggregation-induced enhanced luminescence from the instantaneous aggregates formed by **1a**−**c** and **1d-FA** in a DMSO/water mixture solution. Varying side chains attached on the cyanostilbene core from hydrophobic to hydrophilic units induces the morphology tuning of aggregates with different sizes. The aggregates **1c**$_{(agg)}$ and **1d-FA**$_{(agg)}$ formed from the derivatives with hydrophilic side chains, *i.e.*, glycol and FA-attached glycol, show spherical morphology. All aggregates exhibit hitherto unreported three-photon excited luminescence properties, and the aggregate **1d-FA**$_{(agg)}$ presents the highest 3PA cross-section value among all the derivatives. We have then demonstrated the targeted three-photon bioimaging capability of **1d-FA**$_{(agg)}$ in comparison with **1c**$_{(agg)}$ using healthy and cancerous cell lines. The enhanced targeting of **1d-FA**$_{(agg)}$ to HeLa cancer cells has been achieved through the folate receptor-mediated endocytosis. Thus, this study presents a novel paradigm of using organic nanoaggregates for targeted high-resolution three-photon bioimaging *in vitro*.

METHODS

Quantum Yield Measurements. Fluorescence quantum yields were measured by the relative comparison procedure using quinine sulfate with a quantum yield of 0.54 in 0.1 M H_2SO_4 as reference compound. The quantum yield was calculated from eq 1 shown below

$$\phi_f = \phi_f'(I_{sample}/I_{std})(A_{std}/A_{sample})(n^2{}_{sample}/n^2{}_{std}) \quad (1)$$

where ϕ_f' is the absolute quantum yield of the reference compound, I_{sample} and I_{std} are the integrated emission intensities, A_{sample} and A_{std} are the absorbance at the excitation wavelength, and $n^2{}_{sample}$ and $n^2{}_{std}$ are the respective refractive indices.

Calculation of Refractive Indices. To calculate the quantum yields and the 3PA cross-section, the refractive index of the mixture solvent (DMSO/water) was employed, as we used it to prepare the corresponding solution. To calculate the refractive index of the mixture solution, the following eq 2 was used

$$n = \frac{n_{water}V_{water} + n_{DMSO}V_{DMSO}}{V_{water} + V_{DMSO}} \quad (2)$$

where n_{water} and n_{DMSO} are the refractive indices of water and DMSO and V is their respective volume in the mixture. Considering n_{water} and n_{DMSO} of water and DMSO are 1.33 and 1.479, respectively, the refractive indices of mixture solvent used to form the aggregates for **1a**−**c** and **1d-FA** were calculated to be 1.39, 1.34, 1.34, and 1.34, respectively.

Measurements of 3PA Cross-Section. 3PA spectra of the samples were obtained by using a multiphoton luminescence method with rhodamine B in water as the reference. A Ti:sapphire system that produces a 100 fs (HW1/e) pulse in the wavelength range of 260−2600 nm with a repetition of 1000 Hz was used as the excitation source. In the measurement process, the input laser beam was focused into the solutions. To avoid the self-reabsorption in the 3PA cross-section measurements, the laser beam was focused as close as possible to the wall of the quartz cell and the luminescence signal was collected in backscattering geometry, so that only the emission from the edge of the solution was collected. Thus, an optimal distance between excitation source and sample was maintained during all measurements. Considering the same emitted photon collection efficiency for all the samples, the luminescence intensity ratio of F_3 to F_2 can be further expressed as

$$\frac{F_3}{F_2} = \frac{\eta_3\sigma_3N_3I_0^3}{\eta_2\sigma_2N_2I_0^2} = \frac{\eta_3\sigma_3C_3V_3I_0^3}{\eta_2\sigma_2C_2V_2I_0^2} \quad (3)$$

where, F_3 and F_2 are the three- and two-photon excited luminescence intensity respectively, η is the photoluminescence quantum efficiency, σ_3 and σ_2 are the 3PA cross-section of the samples and

2PA cross-section of rhodamine B, respectively, I_0 is the incident intensity at the focus, V_3 and V_2 are the effective focal volumes of the three-photon-excited samples and the two-photon-excited rhodamine B, respectively, and C_3 and C_2 are the molar concentrations of samples and Rhodamine B, respectively.

The effective volume[58] of the two- and three-photon excitations can be, respectively, approximated as

$$V_3 = 2^3(\pi)^{3/2}3^{-3/2}\omega_0^3 L \quad (4)$$

$$V_2 = (2\pi)^{3/2}\omega_0^3 L \quad (5)$$

where L describes the elongation of the volume along the optical axis, while ω_0 describes the spot size at the focus. Therefore, eq 6 could be derived:

$$\frac{F_3}{F_2} = \frac{0.54\eta_3\sigma_3 C_3 I_0}{\eta_2\sigma_2 C_2} \quad (6)$$

By comparing the three-photon excited fluorescence intensity of samples with the two-photon excited fluorescence intensity of rhodamine B, their quantum yields, molar concentrations, and the values of the 3PA cross-section were achieved.

Cell Culture. HeLa, MCF7, and HEK293 cells were seeded and grown in DMEM supplemented with 10% fetal bovine serum at 37 °C. These samples were trypsinized, and about 1×10^4 cells were added in each well of a 6-well culture plate. After 24 h of growth, all of the cell lines were incubated with solutions (47.5 μM) of the nanoaggregates **1c**$_{(agg)}$ and **1d-FA**$_{(agg)}$ at 37 °C in the culture medium for 4 h. After being washed with phosphate-buffered saline three times to remove remaining nanoaggregates, cells were viewed under a fluorescence microscope (IX7, inverted fluorescent microscope, Olympus) at an excitation of 1300 nm using a band gap filter with a wavelength range of 500−600 nm to block excited light.

MTT Assay for Cytotoxicity Studies. To investigate the cytotoxicity of **1c**$_{(agg)}$ and **1d-FA**$_{(agg)}$ on HeLa, MCF7, and HEK293 cell lines, a conventional MTT assay was used.[59] All of the cell lines were seeded into a 96-well plate at a density of 1×10^4 cells/well in DMEM. After 24 h exposure, the medium in the wells was replaced with fresh medium (100 μL) containing **1c**$_{(agg)}$ and **1d-FA**$_{(agg)}$, with gradually diluted concentrations according to standard procedure. After incubation for another 24 h, the medium was removed, and a medium (100 μL) containing MTT (0.5 mg mL^{-1}) was added. After further incubation for 4 h, the medium was replaced with DMSO (100 μL). The plate was gently shaken for 30 min, and then the absorbance at 560 nm was recorded using a microplate reader (infinite 200 PRO, Tecan). The cell viability related to the control wells that only contain cell culture medium was calculated by $[A]_{test}/[A]_{control}$, where $[A]_{test}$ and $[A]_{control}$ are the average absorption intensities of the test and control samples, respectively.

Conflict of Interest: The authors declare no competing financial interest.

Supporting Information Available: Detailed experimental procedures and additional characterization data including copies of NMR and mass spectra. The Supporting Information is available free of charge on the ACS Publications website at DOI: 10.1021/nn507072r.

Acknowledgment. This research is supported by the National Research Foundation (NRF), Prime Minister's Office, Singapore, under its NRF Fellowship (NRF2009NRF-RF001-015), Campus for Research Excellence and Technological Enterprise (CREATE) Programme − Singapore Peking University Research Centre for a Sustainable Low-Carbon Future, and Competitive Research Programme (CRP) under Project No. NRF-CRP5-2009-04, as well as the NTU-A*Star Silicon Technologies Centre of Excellence under Program No. 112 351 0003. The work was also partially supported by the National Science Foundation of China (NSFC Grant No. 11404219).

REFERENCES AND NOTES

1. Moriyama, E. H.; Zheng, G.; Wilson, B. C. Optical Molecular Imaging: From Single Cell to Patient. *Clin. Pharmacol. Ther.* **2008**, *84*, 267–271.
2. Weissleder, R.; Pittet, M. J. Imaging in the Era of Molecular Oncology. *Nature* **2008**, *452*, 580–589.
3. Thekkek, N.; Richards-Kortum, R. Optical Imaging for Cervical Cancer Detection: Solutions for a Continuing Global Problem. *Nat. Rev. Cancer* **2008**, *8*, 725–731.
4. Tian, Z.; Li, A. D. Q. Photoswitching-Enabled Novel Optical Imaging: Innovative Solutions for Real-World Challenges in Fluorescence Detections. *Acc. Chem. Res.* **2012**, *46*, 269–279.
5. Webb, R. H. Theoretical Basis of Confocal Microscopy. In *Methods in Enzymology*; Conn, P. M., Ed.; Academic Press: New York, 1999; vol. 307, pp 3−20.
6. Ntziachristos, V. Going Deeper Than Microscopy: The Optical Imaging Frontier in Biology. *Nat. Meth.* **2010**, *7*, 603–614.
7. Denk, W.; Strickler, J.; Webb, W. Two-Photon Laser Scanning Fluorescence Microscopy. *Science* **1990**, *248*, 73–76.
8. Xu, C.; Zipfel, W.; Shear, J. B.; Williams, R. M.; Webb, W. W. Multiphoton Fluorescence Excitation: New Spectral Windows for Biological Nonlinear Microscopy. *Proc. Natl. Acad. Sci. U.S.A.* **1996**, *93*, 10763–10768.
9. Xu, C.; Williams, R. M.; Zipfel, W.; Webb, W. W. Multiphoton Excitation Cross-Sections of Molecular Fluorophores. *Bioimaging* **1996**, *4*, 198–207.
10. Maiti, S.; Shear, J. B.; Williams, R. M.; Zipfel, W. R.; Webb, W. W. Measuring Serotonin Distribution in Live Cells with Three-Photon Excitation. *Science* **1997**, *275*, 530–532.
11. Zipfel, W. R.; Williams, R. M.; Webb, W. W. Nonlinear Magic: Multiphoton Microscopy in the Biosciences. *Nat. Biotechnol.* **2003**, *21*, 1369–1377.
12. Zipfel, W. R.; Williams, R. M.; Christie, R.; Nikitin, A. Y.; Hyman, B. T.; Webb, W. W. Live Tissue Intrinsic Emission Microscopy Using Multiphoton-Excited Native Fluorescence and Second Harmonic Generation. *Proc. Natl. Acad. Sci. U.S.A.* **2003**, *100*, 7075–7080.
13. Levene, M. J.; Dombeck, D. A.; Kasischke, K. A.; Molloy, R. P.; Webb, W. W. *In Vivo* Multiphoton Microscopy of Deep Brain Tissue. *J. Neurophysiol.* **2004**, *91*, 1908–1912.
14. Helmchen, F.; Denk, W. Deep Tissue Two-Photon Microscopy. *Nat. Meth.* **2005**, *2*, 932–940.
15. Sreejith, S.; Huong, T. T. M.; Borah, P.; Zhao, Y. L. Organic-Inorganic Nanohybrids for Fluorescence, Photoacoustic and Raman Bioimaging. *Sci. Bull.* **2015**, *60*, 665–678.
16. He, G. S.; Tan, L.-S.; Zheng, Q.; Prasad, P. N. Multiphoton Absorbing Materials: Molecular Designs, Characterizations, and Applications. *Chem. Rev.* **2008**, *108*, 1245–1330.
17. He, T.; Too, P. C.; Chen, R.; Chiba, S.; Sun, H. Concise Synthesis and Two-Photon-Excited Deep-Blue Emission of 1,8-Diazapyrenes. *Chem.—Asian J.* **2012**, *7*, 2090–2095.
18. He, T.; Lim, Z. B.; Ma, L.; Li, H.; Rajwar, D.; Ying, Y.; Di, Z.; Grimsdale, A. C.; Sun, H. Large Two-Photon Absorption of Terpyridine-Based Quadrupolar Derivatives: Towards their Applications in Optical Limiting and Biological Imaging. *Chem.—Asian J.* **2013**, *8*, 564–571.
19. He, T.; Sreejith, S.; Gao, Y.; Grimsdale, A. C.; Zhao, Y. L.; Sun, H. Superior Optical Nonlinearity of an Exceptional Fluorescent Stilbene Dye. *Appl. Phys. Lett.* **2015**, *106*, 111904.
20. Horton, N. G.; Wang, K.; Kobat, D.; Clark, C. G.; Wise, F. W.; Schaffer, C. B.; Xu, C. *In Vivo* Three-Photon Microscopy of Subcortical Structures within an Intact Mouse Brain. *Nat. Photonics* **2013**, *7*, 205–209.
21. Yu, J. H.; Kwon, S.-H.; Petrášek, Z.; Park, O. K.; Jun, S. W.; Shin, K.; Choi, M.; Park, Y. I.; Park, K.; Na, H. B.; et al. High-Resolution Three-Photon Biomedical Imaging Using Doped ZnS Nanocrystals. *Nat. Mater.* **2013**, *12*, 359–366.
22. Cho, S. J.; Maysinger, D.; Jain, M.; Röder, B.; Hackbarth, S.; Winnik, F. M. Long-Term Exposure to CdTe Quantum Dots Causes Functional Impairments in Live Cells. *Langmuir* **2007**, *23*, 1974–1980.
23. Smith, A. M.; Duan, H.; Mohs, A. M.; Nie, S. Bioconjugated Quantum Dots for *in Vivo* Molecular and Cellular Imaging. *Adv. Drug Delivery Rev.* **2008**, *60*, 1226–1240.
24. Yong, K.-T.; Roy, I.; Ding, H.; Bergey, E. J.; Prasad, P. N. Biocompatible Near-Infrared Quantum Dots as Ultrasensitive

Probes for Long-Term *in Vivo* Imaging Applications. *Small* **2009**, *5*, 1997–2004.
25. Hauck, T. S.; Anderson, R. E.; Fischer, H. C.; Newbigging, S.; Chan, W. C. W. *In Vivo* Quantum-Dot Toxicity Assessment. *Small* **2010**, *6*, 138–144.
26. Chen, N.; He, Y.; Su, Y.; Li, X.; Huang, Q.; Wang, H.; Zhang, X.; Tai, R.; Fan, C. The Cytotoxicity of Cadmium-Based Quantum Dots. *Biomaterials* **2012**, *33*, 1238–1244.
27. Yong, K.-T.; Law, W.-C.; Hu, R.; Ye, L.; Liu, L.; Swihart, M. T.; Prasad, P. N. Nanotoxicity Assessment of Quantum Dots: From Cellular to Primate Studies. *Chem. Soc. Rev.* **2013**, *42*, 1236–1250.
28. Clift, M. J. D.; Boyles, M. S. P.; Brown, D. M.; Stone, V. An Investigation into the Potential for Different Surface-Coated Quantum Dots to Cause Oxidative Stress and Affect Macrophage Cell Signaling *in Vitro*. *Nanotoxicology* **2010**, *4*, 139–149.
29. Derfus, A. M.; Chan, W. C. W.; Bhatia, S. N. Probing the Cytotoxicity of Semiconductor Quantum Dots. *Nano Lett.* **2003**, *4*, 11–18.
30. Kirchner, C.; Liedl, T.; Kudera, S.; Pellegrino, T.; Muñoz Javier, A.; Gaub, H. E.; Stölzle, S.; Fertig, N.; Parak, W. J. Cytotoxicity of Colloidal CdSe and CdSe/ZnS Nanoparticles. *Nano Lett.* **2004**, *5*, 331–338.
31. Li, J. L.; Goh, C. C.; Keeble, J. L.; Qin, J. S.; Roediger, B.; Jain, R.; Wang, Y.; Chew, W. K.; Weninger, W.; Ng, L. G. Intravital Multiphoton Imaging of Immune Responses in the Mouse Ear Skin. *Nat. Protocols* **2012**, *7*, 221–234.
32. Marks, K. M.; Nolan, G. P. Chemical Labeling Strategies for Cell Biology. *Nat. Meth.* **2006**, *3*, 591–596.
33. Chithrani, B. D.; Chan, W. C. W. Elucidating the Mechanism of Cellular Uptake and Removal of Protein-Coated Gold Nanoparticles of Different Sizes and Shapes. *Nano Lett.* **2007**, *7*, 1542–1550.
34. Christophe Youta, D.; Maya, K.; Rima, Z.; Regis, M.; Didier, B. Characterization of Endocytosis and Exocytosis of Cationic Nanoparticles in Airway Epithelium Cells. *Nanotechnology* **2010**, *21*, 355102.
35. Ding, D.; Li, K.; Liu, B.; Tang, B. Z. Bioprobes Based on AIE Fluorogens. *Acc. Chem. Res.* **2013**, *46*, 2441–2453.
36. Li, K.; Qin, W.; Ding, D.; Tomczak, N.; Geng, J.; Liu, R.; Liu, J.; Zhang, X.; Liu, H.; Liu, B.; Tang, B. Z. Photostable Fluorescent Organic Dots with Aggregation-Induced Emission (AIE Dots) for Noninvasive Long-Term Cell Tracing. *Sci. Rep.* **2013**, *3*, 1150.
37. Ding, D.; Goh, C. C.; Feng, G.; Zhao, Z.; Liu, J.; Liu, R.; Tomczak, N.; Geng, J.; Tang, B. Z.; Ng, L. G.; Liu, B. Ultrabright Organic Dots with Aggregation-Induced Emission Characteristics for Real-Time Two-Photon Intravital Vasculature Imaging. *Adv. Mater.* **2013**, *25*, 6083–6088.
38. Wu, C.; Bull, B.; Szymanski, C.; Christensen, K.; McNeill, J. Multicolor Conjugated Polymer Dots for Biological Fluorescence Imaging. *ACS Nano* **2008**, *2*, 2415–2423.
39. Kaeser, A.; Schenning, A. P. H. J. Fluorescent Nanoparticles Based on Self-Assembled π-Conjugated Systems. *Adv. Mater.* **2010**, *22*, 2985–2997.
40. Petkau, K.; Kaeser, A.; Fischer, I.; Brunsveld, L.; Schenning, A. P. H. J. Pre- and Postfunctionalized Self-Assembled π-Conjugated Fluorescent Organic Nanoparticles for Dual Targeting. *J. Am. Chem. Soc.* **2011**, *133*, 17063–17071.
41. Kaeser, A.; Fischer, I.; Abbel, R.; Besenius, P.; Dasgupta, D.; Gillisen, M. A. J.; Portale, G.; Stevens, A. L.; Herz, L. M.; Schenning, A. P. H. J. Side Chains Control Dynamics and Self-Sorting in Fluorescent Organic Nanoparticles. *ACS Nano* **2012**, *7*, 408–416.
42. An, B.-K.; Kwon, S.-K.; Jung, S.-D.; Park, S. Y. Enhanced Emission and Its Switching in Fluorescent Organic Nanoparticles. *J. Am. Chem. Soc.* **2002**, *124*, 14410–14415.
43. An, B.-K.; Lee, D.-S.; Lee, J.-S.; Park, Y.-S.; Song, H.-S.; Park, S. Y. Strongly Fluorescent Organogel System Comprising Fibrillar Self-Assembly of a Trifluoromethyl-Based Cyanostilbene Derivative. *J. Am. Chem. Soc.* **2004**, *126*, 10232–10233.
44. Yoon, S.-J.; Chung, J. W.; Gierschner, J.; Kim, K. S.; Choi, M.-G.; Kim, D.; Park, S. Y. Multistimuli Two-Color Luminescence Switching *via* Different Slip-Stacking of Highly Fluorescent Molecular Sheets. *J. Am. Chem. Soc.* **2010**, *132*, 13675–13683.
45. Wang, B.; Wang, Y.; Hua, J.; Jiang, Y.; Huang, J.; Qian, S.; Tian, H. Starburst Triarylamine Donor−Acceptor−Donor Quadrupolar Derivatives Based on Cyano-Substituted Diphenylaminestyrylbenzene: Tunable Aggregation-Induced Emission Colors and Large Two-Photon Absorption Cross Sections. *Chem.—Eur. J.* **2011**, *17*, 2647–2655.
46. Parthasarathy, V.; Fery-Forgues, S.; Campioli, E.; Recher, G.; Terenziani, F.; Blanchard-Desce, M. Dipolar *versus* Octupolar Triphenylamine-Based Fluorescent Organic Nanoparticles as Brilliant One- and Two-Photon Emitters for (Bio)imaging. *Small* **2011**, *7*, 3219–3229.
47. Cohanoschi, I.; Barbot, A.; Belfield, K. D.; Yao, S.; Hernandez, F. E. Mega Three-Photon Absorption Cross-Section Enhancement in Pseudoisocyanine *J*-Aggregates. *J. Chem. Phys.* **2005**, *123*, 231104.
48. Wu, P. L.; Feng, X. J.; Tam, H. L.; Wong, M. S.; Cheah, K. W. Efficient Three-Photon Excited Deep Blue Photoluminescence and Lasing of Diphenylamino and 1,2,4-Triazole Endcapped Oligofluorenes. *J. Am. Chem. Soc.* **2008**, *131*, 886–887.
49. Cronstrand, P.; Jansik, B.; Jonsson, D.; Luo, Y.; Ågren, H. Density Functional Response Theory Calculations of Three-Photon Absorption. *J. Chem. Phys.* **2004**, *121*, 9239–9246.
50. Mandal, A. K.; He, T.; Maji, S. K.; Sun, H.; Zhao, Y. A Three-Photon Probe with Dual Emission Colors for Imaging of Zn(II) Ions in Living Cells. *Chem. Commun.* **2014**, *50*, 14378–14381.
51. Feldmann, J.; Peter, G.; Göbel, E. O.; Dawson, P.; Moore, K.; Foxon, C.; Elliott, R. J. Linewidth Dependence of Radiative Exciton Lifetimes in Quantum Wells. *Phys. Rev. Lett.* **1987**, *59*, 2337–2340.
52. Spano, F. C.; Mukamel, S. Superradiance in Molecular Aggregates. *J. Chem. Phys.* **1989**, *91*, 683–700.
53. De Boer, S.; Wiersma, D. A. Dephasing-Induced Damping of Superradiant Emission in J-Aggregates. *Chem. Phys. Lett.* **1990**, *165*, 45–53.
54. An, B.-K.; Gierschner, J.; Park, S. Y. π-Conjugated Cyanostilbene Derivatives: A Unique Self-Assembly Motif for Molecular Nanostructures with Enhanced Emission and Transport. *Acc. Chem. Res.* **2011**, *45*, 544–554.
55. Collini, E. Cooperative Effects to Enhance Two-Photon Absorption Efficiency: Intra- *versus* Inter-Molecular Approach. *Phys. Chem. Chem. Phys.* **2012**, *14*, 3725–3736.
56. Zhang, Q.; Wang, X.; Li, P.-Z.; Nguyen, K. T.; Wang, X.-J.; Luo, Z.; Zhang, H.; Tan, N. S.; Zhao, Y. Biocompatible, Uniform, and Redispersible Mesoporous Silica Nanoparticles for Cancer-Targeted Drug Delivery *in Vivo*. *Adv. Funct. Mater.* **2014**, *24*, 2450–2461.
57. Ma, X.; Sreejith, S.; Zhao, Y. Spacer Intercalated Disassembly and Photodynamic Activity of Zinc Phthalocyanine Inside Nanochannels of Mesoporous Silica Nanoparticles. *ACS Appl. Mater. Interfaces* **2013**, *5*, 12860–12868.
58. Elson, E. L. Fluorescence Correlation Spectroscopy. *Theory and Applications*; Springer: New York, 2001.
59. Sreejith, S.; Ma, X.; Zhao, Y. Graphene Oxide Wrapping on Squaraine-Loaded Mesoporous Silica Nanoparticles for Bioimaging. *J. Am. Chem. Soc.* **2012**, *134*, 17346–17349.